

The Nucleon Axial-Vector Form Factor at the Physical Point with the HISQ Ensembles

A. Bazavov,¹ C. Bernard,² C. DeTar,³ A. X. El-Khadra,^{4,5} E. Gámiz,⁶ Steven Gottlieb,⁷
U. M. Heller,⁸ R. J. Hill,^{9,5} C. Hughes,⁵ A. S. Kronfeld,^{5,*} J. Laiho,¹⁰ Ruizhi Li,⁷
Yin Lin,^{11,5} P. B. Mackenzie,⁵ A. S. Meyer,^{12,†} E. T. Neil,^{13,14} J. Osborn,¹⁵ J. Simone,⁵
A. Strelchenko,⁵ R. Sugar,¹⁶ D. Toussaint,¹⁷ R. S. Van de Water,⁵ and A. Veernala⁵

(Fermilab Lattice and MILC Collaborations)

¹*Michigan State University, East Lansing, Michigan, USA*

²*Washington University, St. Louis, Missouri, USA*

³*University of Utah, Salt Lake City, Utah, USA*

⁴*University of Illinois, Urbana, Illinois, USA*

⁵*Fermi National Accelerator Laboratory, Batavia, Illinois, USA*

⁶*Universidad de Granada, Granada, Spain*

⁷*Indiana University, Bloomington, Indiana, USA*

⁸*American Physical Society, Ridge, New York, USA*

⁹*University of Kentucky, Lexington, Kentucky, USA*

¹⁰*Syracuse University, Syracuse, New York, USA*

¹¹*University of Chicago, Chicago, Illinois, USA*

¹²*Brookhaven National Laboratory, Upton, New York, USA*

¹³*University of Colorado, Boulder, Colorado, USA*

¹⁴*RIKEN-BNL Research Center, Upton, New York, USA*

¹⁵*Argonne National Laboratory, Argonne, Illinois, USA*

¹⁶*University of California, Santa Barbara, California, USA*

¹⁷*University of Arizona, Tucson, Arizona, USA*

(Dated: March 2, 2018)

Abstract

We propose to continue our computation of the axial-vector form factor of the nucleon using the highly-improved staggered-quark (HISQ) action for both valence and sea quarks. We use the (2+1+1)-flavor HISQ ensembles generated at the physical point, combining lattice QCD calculations of the q^2 dependence with the z expansion to obtain a model-independent description of the shape. As a by-product, we will compute the axial charge g_A directly at the physical point. We will test our approach with the shape of the vector form factor, which is constrained by high-statistics electron-scattering data. The project is well aligned with USQCD goals, because the axial-vector form factor is an important ingredient in quasielastic neutrino-nucleon scattering, which is the key signal process in neutrino-oscillation experiments at Fermilab.

We request 832 k K40-GPU-hours and 53 M Jpsi-core-hours at BNL or Fermilab; we also request 50 Tbyte disk space and 168 Tbyte tape storage. If we continue running at BNL and the tape storage has to be at Fermilab, some scratch space at Fermilab for staging is also needed. Using USQCD conversion factors, the total request is 241 M Jpsi-core-hours.

Editing colors: *Aaron*, *Alexei*, *Andreas*, *Ciaran*, *Jim*, *Yin*, and *new material for collaborators*.

* ask@fnal.gov

† ameyer@quark.phy.bnl.gov

I. INTRODUCTION

In 2014, the Particle Physics Project Prioritization Panel (P5) recommended a suite of short- and long-baseline neutrino experiments as the core of the coming, domestic, accelerator-based high-energy physics program [1]. The main motivations are to answer questions that explore beyond the Standard Model: What are the neutrino mass and oscillation parameters, including CP violation? Are neutrinos Majorana particles? Are there additional sterile species of neutrino? Do neutrinos interact in non-Standard ways, for example as they pass through matter? Since 2015, Fermilab and its partners have taken several steps toward answering these questions, with results from NOvA, installation and operation of MicroBooNE, refurbishment of ICARUS at CERN, and establishment of a strong international collaboration for the future long-baseline DUNE experiment.

These questions sound remote from QCD, but the essence of the experimental technique is neutrino-nucleus scattering. Until recently, the goal has been to demonstrate that neutrino mixing parameters are nonzero, and neutrino-oscillation experiments (mostly) circumvented hadronic and nuclear physics with measurements of $\text{flux} \times (\text{cross section})$ from a near detector. Now that experiments are moving from first observations to precise measurements, the theoretical understanding of the neutrino-nucleus interaction will play an ever more important role.

Figure 1 depicts the interplay of nuclear physics, hadronic physics, and neutrino physics. The key signal process is charged-current quasielastic scattering, $\nu_l n \rightarrow l^- p$ (or $\bar{\nu}_l p \rightarrow l^+ n$), i.e., with no extra pions. As it stands (Fig. 1, left), scattering data must be analyzed assuming both a form-factor model for the nucleon-level transition and nuclear models. The latter describe the initial state of the nucleon inside the nucleus and also how final-state interactions with the nucleus modify the signal. For example, primary pions could be absorbed by the nucleus, or secondary pions could be created after the initial scatter. The experimental data are then studied further, often with a Monte Carlo such as GENIE [2], to look for self-consistency of the hadronic and nuclear models. Even when this process converges to a stable description of the data, it introduces an unquantifiable uncertainty into estimates of neutrino-oscillation parameters, θ_{ij} and δ_{CP} .

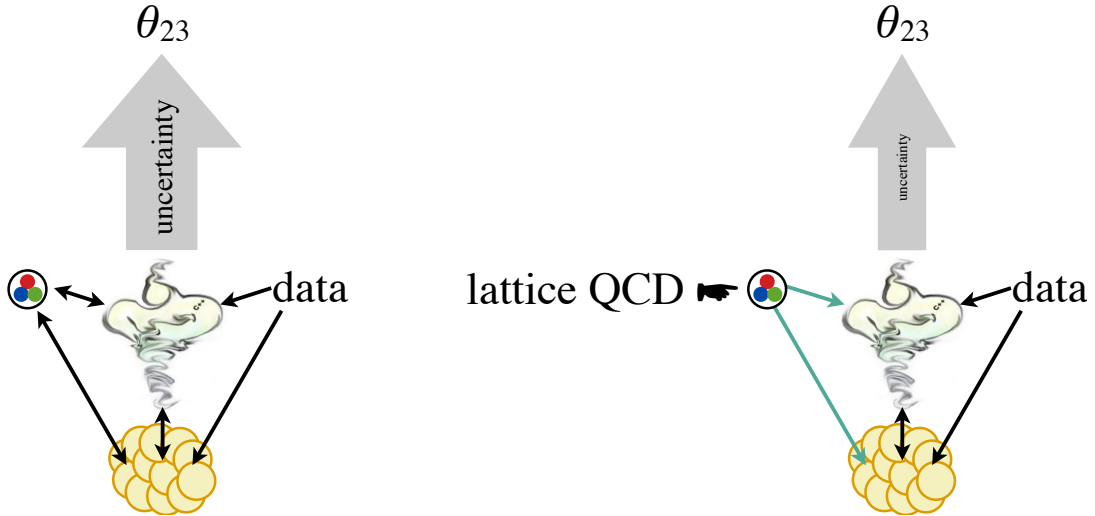


FIG. 1. Left: current interplay between data, hadronic physics (circle enclosing a red, green, and blue quark), and nuclear physics (collection of nucleons at the bottom), feeding into the GENIE Monte Carlo [2] and ultimately uncertainties on oscillation parameters, such as θ_{23} . Right: sketch of the disruption possible with *ab initio* calculations from lattice QCD.

The neutrino-nucleon interaction can be understood, from first principles, with lattice QCD. Nucleon physics is a challenge, so (for now) we address the obvious first step: a calculation of the shape of the axial-vector form factor. Calculations of this form factor have a considerable history in lattice QCD and have been found to be much more demanding than those of meson form factors. Some of the challenges are a difficult chiral extrapolation, large finite-volume effects, and contamination from excited states in lattice-QCD correlation functions. We address the first two problems with the HISQ ensembles [3, 4]. We propose to start with the physical-point ensembles, so no chiral extrapolation will be needed. The physical volumes of these ensembles are large: $L > 5$ fm, $3.3 \leq M_\pi L \leq 3.9$. Thus, finite-volume effects should be under control. Previous work [5–12], by contrast, has had $L < 3$ fm for most, if not all, ensembles. With our allocation for AY 2016–2017, we have demonstrated sub-percent errors on nucleon and Δ masses and find excellent isolation and precision on $N\pi$ scattering states, as discussed in Sec. V. As this and other *ab initio* calculations of the neutrino-nucleon interaction are brought into the picture, hadronic physics can inform the data and the nuclear modeling. The long-term goal is to combine these calculations with better nuclear models, to help the experiments reach their goals of precise measurements of neutrino mixing angles and mass-square differences.

II. METHODS

Neutrino-nucleon scattering is mediated by W -boson exchange. In quasielastic scattering, we are interested in the matrix elements

$$\langle p(\mathbf{p}) | \mathcal{V}_\mu^+ | n(\mathbf{k}) \rangle = \bar{u}_p(\mathbf{p}) \left[\gamma_\mu F_1(q^2) + \frac{i\sigma_{\mu\nu} q^\nu}{2M_N} F_2(q^2) \right] u_n(\mathbf{k}), \quad (2.1)$$

$$\langle p(\mathbf{p}) | \mathcal{A}_\mu^+ | n(\mathbf{k}) \rangle = \bar{u}_p(\mathbf{p}) \left[\left(\gamma_\mu - \frac{2M_N q_\mu}{q^2} \right) \gamma^5 F_A(q^2) + \frac{2M_N q_\mu}{q^2} \gamma^5 F_P(q^2) \right] u_n(\mathbf{k}), \quad (2.2)$$

where \bar{u}_p and u_n are nucleon spinor wave functions, \mathcal{V}_μ^+ and \mathcal{A}_μ^+ are the charged (continuum) vector and axial-vector currents, respectively, M_N is the nucleon mass (neglecting isospin), and $q = p - k$ is the momentum transfer. Neutrino physics needs the axial form factor $F_A(q^2)$, while the vector form factor $F_1(q^2)$ can be used to build confidence in our results, because its shape is constrained (up to isospin violation) by high-statistics electron-nucleon scattering. In neutrino scattering, the form factors F_2 and F_P are not as important as F_1 and F_A .

A. Staggered Baryon Operators

Operators for baryons with staggered quarks have been studied in the past [13, 14]. In general, composite operators of staggered fields with good quantum numbers are spread over a 2^3 -site cube on a timeslice t . One introduces

$$\psi_{iA}^a(y) = \chi_i^a(y + A), \quad (2.3)$$

where χ is the one-component field in the staggered action (of color a and flavor i). The coordinate y labels the origin of the cubes (and $y_4 = t$), and A is a sum of unit vectors connecting y to the other corners of the spatial cube. One then introduces a basic trilinear [13, 14]

$$_{ijk} \mathcal{B}_{ABC}(y) = \epsilon^{abc} \psi_{iA}^a(y) \psi_{jB}^b(y) \psi_{kC}^c(y) \quad (2.4)$$

that has been antisymmetrized over color. Gauge symmetry can be enforced by inserting gauge links on a path from $y + A$ back to y or, for A consisting of 2 or 3 directions, an average over various paths. We use Coulomb gauge for corner wall sources (see below), which inserts implicit averages over many paths.

Generic baryon two-point and three-point correlators are then

$${}_{ijk\bar{i}\bar{j}\bar{k}}C_{ABC\bar{A}\bar{B}\bar{C}}(t) = \frac{1}{N_s^3} \sum_{\mathbf{y}} \langle {}_{ijk}\mathcal{B}_{ABC}(\mathbf{y}) {}_{\bar{i}\bar{j}\bar{k}}\bar{\mathcal{B}}_{\bar{A}\bar{B}\bar{C}}(z) \rangle, \quad (2.5)$$

$${}_{ijk\bar{i}\bar{j}\bar{k}}C_{ABC\bar{A}\bar{B}\bar{C}}^\mu(t, \tau) = \frac{1}{N_s^6} \sum_{\mathbf{x}, \mathbf{y}} e^{i\mathbf{p} \cdot (\mathbf{x} - \mathbf{y})} \langle {}_{ijk}\mathcal{B}_{ABC}(\mathbf{y}) A^\mu(\mathbf{x}) {}_{\bar{i}\bar{j}\bar{k}}\bar{\mathcal{B}}_{\bar{A}\bar{B}\bar{C}}(z) \rangle, \quad (2.6)$$

with N_s^3 lattices, Euclidean times $x_4 = \tau$, $y_4 = t$, and origin (for now) $z = 0$. The lattice axial current, $A^\mu(\mathbf{x})$, is a bilinear of the staggered-fermion field. $\bar{\mathcal{B}}$ is constructed by replacing quark fields in Eq. (2.4) with antiquark fields. In practice, the \mathcal{B} and $\bar{\mathcal{B}}$ operators are contracted with coefficient tensors ${}^{ijk}\mathcal{O}_r^{RABC}$ and $\bar{i}\bar{j}\bar{k}\bar{\mathcal{O}}_{\bar{r}}^{\bar{R}\bar{A}\bar{B}\bar{C}}$, where r and \bar{r} label the irreducible representation (irrep) of the staggered-fermion symmetry group, and R and \bar{R} label the component within the irrep. Below, we refer to sums over (A, B, C) and $(\bar{A}, \bar{B}, \bar{C})$ as “tie-ups.” As discussed in Sec. II B, the construction of Ref. [14] yields several operators for each irrep r .

As discussed in previous proposals, we start with the corner-wall source [15–18], solving

$$(D + m)_{AC}^{ac} G_{CB}^{cb}(\mathbf{y}, z_4) = \delta^{ab} \delta_{y_4, z_4} \sum_{\mathbf{z}} \delta_{\mathbf{y} + \mathbf{A}, \mathbf{z} + \mathbf{B}}, \quad (2.7)$$

where, as above, \mathbf{y} (\mathbf{y}) and \mathbf{z} (\mathbf{z}) denote the coordinates of (hyper)cubes, and A, B, C the location within spatial cubes. Here, a and b are color indices. **These propagators continue to play a central role. Because the previous two allocation years’ propagators are stored on tape,¹ we can continue to use them.**

Last year, we proposed to compute corner-wall propagators at the sink using noise on the right-hand side [19]. The daughter-quark propagator, flowing from the current at x to the sink at y , was the complex conjugate of this propagator from the sink back to the current. For the two-point function, we found that this method worked just as well as a wall-to-point correlator composed of three propagators $G_{CB}^{cb}(\mathbf{y}, z_4)$ from Eq. (2.7). We expected the same to hold for the three-point function, because the wall+current is itself a wall source with some decoration (especially when the current’s timeslice is close to z_4). This is not the case: after tracking all sums over timeslices for signal and noise, one finds that the signal-to-noise volume averaging degrades from $O(N_s^{3/2})$ to $O(1)$. Our efforts to understand this problem led to underutilization of our allocation in the first quarter of this allocation year.

We therefore switched to two different strategies, both of which use a sequential propagator from the current for the daughter quark in the three-point function. The first strategy, which we call the corner current, puts the local current at a single corner, D , of the unit cube, solving

$$(D + m)_{AC}^{ac} \hat{G}_{CB;q,D}^{cb}(x, y_4, z_4) = \delta^{ab} \delta_{x_4, y_4} \sum_{\mathbf{y}} \delta_{\mathbf{x} + \mathbf{A}, \mathbf{y} + \mathbf{D}} e^{-i\mathbf{q} \cdot (\mathbf{y} + \mathbf{D})} G_{DB}^{cb}(\mathbf{y}, z_4), \quad (2.8)$$

where the parent propagator $G_{DB}^{cb}(\mathbf{y}, z_4)$ is computed from Eq. (2.7). In practice, we choose the corner for the current insertion at random from one configuration to the next. The different choices

¹ A few from the smallest lattices have not been kept but are cheap to recompute.

of D are later summed with correct choice of staggered and Fourier phases when performing the ensemble average; we have used it for the zero-momentum vector current, i.e., g_V (ideally = 1). This method has the advantage of flexibility, because all spin-taste currents are accessible. Moreover, it is possible to come back later and fill in the missing corners to improve statistics. Once propagators from all eight corners have been computed, this approach yields information equivalent to our second strategy.

The second strategy, which we call a spin-taste current, explicitly projects the desired spin-taste quantum numbers at the current insertion. This strategy provides an extra factor of 8 statistics in the volume average over the corner-only current of Eq. (2.8) for the same computational cost due to the sum over corners, but fixes the taste of the current insertion. In practice, we do inversions for only the spin-taste current $A^3 \otimes A^3$, which is obtained by applying a relative phase of -1 to sites an odd number of sites away from the origin in the z direction. This current insertion may be obtained by solving the equation

$$(D + m)_{AC}^{ac} \tilde{G}_{CB;q,A_3 \otimes A_3}^{cb}(x, y_4, z_4) = \delta^{ab} \delta_{x_4, y_4} \sum_{D, y} \delta_{x+A, y+D} e^{-iq \cdot (y+D)} (-1)^{D_3} G_{DB}^{cb}(y, z_4), \quad (2.9)$$

Similarly, the local $V^4 \otimes V^4$ vector current requires a similar daughter propagator with $(-1)^{D_3}$ replaced with $(-1)^{D_1+D_2+D_3}$, and so on for other currents. This strategy is more cost effective when a small subset of spin-taste combinations are needed; we have used it for the zero-momentum axial current, i.e., g_A .

A general three-point function can be computed by starting the inversion at $z_4 = 0$ and N_{sep} values of the source-to-insertion time separation, $y_4 - z_4$. An inversion is required for each of N_{mom} choices of momentum and N_{cur} choices of spin-taste- or corner-current insertions. This setup requires

$$N_{\text{inv}} = 8N_c (1 + N_{\text{mom}} N_{\text{cur}} N_{\text{sep}}) \quad (2.10)$$

runs of the (single-color) inverter per configuration, where $N_c = 3$ is the number of colors. Our current plan for the axial charge (and vector charge as a cross check) is to proceed with $N_{\text{mom}} = 1$, $N_{\text{cur}} = 2$, and $N_{\text{sep}} = 4$. For nonzero momentum, we will include an additional $N_{\text{mom}} = 3$ momenta with $N_{\text{sep}} = 4$ and $N_{\text{cur}} = 1$ for a (randomly chosen) corner current only. With additional effective run time (through better hardware, better inverters, or opportunistic running) we will fill in the missing corners, as long as the additional statistics are helpful.

B. Excited States

To discuss our strategy for excited states, it is useful to recall some aspects of the group theory for two or three flavors of staggered fermions [14]. The eight quark fields ψ_A on a spatial cube transform as an 8 under the geometrical timeslice group of staggered fermions (GTS) [13, 14]. The u and d flavors form an isodoublet as always. Baryons thus transform under the tensor product $(8, \frac{1}{2}) \otimes (8, \frac{1}{2}) \otimes (8, \frac{1}{2})$, which can be reduced into a direct sum of irreps, as shown in Table I. The $I = \frac{3}{2}$ ($I = \frac{1}{2}$) column stems from fully symmetric (mixed symmetry) irreps with respect to isospin. Let us refer to states that yield the nucleon (Δ) mass in the continuum limit as “ N -like” (“ Δ -like”). Operators in the irreps $(8, \frac{3}{2})$, $(8, \frac{1}{2})$, $(16, \frac{3}{2})$, and $(16, \frac{1}{2})$ couple to both N -like and Δ -like baryons and, as usual with staggered fermions, parity partners. These four irreps can be used for both three- and two-point functions. Owing to the taste quantum number, N -like states need not have isospin $\frac{1}{2}$ [14]. Operators in the irreps $(8', \frac{3}{2})$ and $(8', \frac{1}{2})$ couple to Δ -like but not N -like states.

TABLE I. Fermionic irreps of $\text{GTS} \times \text{SU}_{\text{isospin}}(2)$ [14]. Colloquially, the different N -like and Δ -like states in each irrep can be called “tastes.”

GTS	isospin:	$\frac{3}{2}$	$\frac{1}{2}$
8		$3N, 2\Delta$	$5N, 1\Delta$
8'		$0N, 2\Delta$	$0N, 1\Delta$
16		$1N, 3\Delta$	$3N, 4\Delta$

The entries in Table I often list more than one taste and kind of state. A useful feature of the construction in Ref. [14] is that several operators arise in each irrep. They differ in the way the quark fields are spread out over the cube. Moreover, the number of operators coincides with the number of distinct baryons in each entry of Table I. For example, in the $(16, \frac{3}{2})$ irrep, we have five baryon operators and, thus, compute a 4×4 matrix correlator. This feature holds throughout Table I. In summary, the structure of the operators mirrors the structure of the states, providing a built-in mechanism to find the nucleon contributions of the correlators.

C. Normalized Axial-Vector Current

In our companion proposal on flavor physics [20], the choice of vector current influences which irreps should be chosen for the mesons at the source and sink of the three-point correlator. For baryons, however, one can use the same irreps, just different components within them. We expect the local axial-vector current, which has axial-vector taste, to be the least noisy. The same staggered baryon multiplets that we use for the two-point analysis, can be used to construct a matrix three-point function in each irrep. Because we are also examining the one-link vector current for $D \rightarrow K\ell\nu$ in the other proposal [20], it is natural to look at the one-link axial-vector current too.

To project out the pseudoscalar form factor, let us define

$$A_{\perp}^{\mu} = A^{\mu} - \frac{q^{\mu}}{q^2} q \cdot A. \quad (2.11)$$

Then, for $q \neq 0$,

$$\langle p(\mathbf{p}) | Z_A A_{\perp}^{\mu} | n(\mathbf{k}) \rangle = \bar{u}_p(\mathbf{p}) \gamma_{\perp}^{\mu} \gamma^5 u_n(\mathbf{k}) F_A(q^2), \quad (2.12)$$

where A^{μ} is the local or one-link lattice current, and Z_A is its matching factor, such that $Z_A A^{\mu}$ and the continuum current \mathcal{A}^{μ} have the same matrix elements.

We can eliminate the matching factor Z_A via ratios. In the case of the axial-vector current, we will form the combination

$$F_A(q^2) \bar{u}_p(\mathbf{p}) \gamma_{\perp}^{\mu} \gamma^5 u_n(\mathbf{k}) = \frac{\langle p(\mathbf{p}) | Z_A A_{\perp}^{\mu} | n(\mathbf{k}) \rangle}{\langle 0 | Z_A A^{\mu} | \pi(0) \rangle \omega^2} \bigg|_{\text{this work}} \frac{\langle 0 | 2\hat{m}P | \pi \rangle}{M_{\pi}} \bigg|_{\text{Ref. [21]}} \omega^2 \big|_{a \rightarrow 0}, \quad (2.13)$$

where P in the second factor is the absolutely normalized pseudoscalar density (with pseudoscalar taste), and ω is a relative scale-setting distance, such as $1/f_{p4s}$ with f_{p4s} the decay constant of meson with quark masses $0.4m_s$ [21], or the gradient-flow [22] length w_0 [23]. The factor Z_A cancels. The pion decay constant from A^{μ} , $\langle 0 | Z_A A^{\mu} | \pi(0) \rangle$, will be calculated as part of this project. The second factor comes from our project on light decay constants [4, 21], as does f_{p4s} . MILC has also published results for the gradient-flow lengths $\sqrt{t_0}$ and w_0 on the HISQ ensembles [24]. Uncertainties in the second and third factors will be subdominant, because they do not entail nucleons. We will use Eq. (2.13) both for g_A , with $\mathbf{p} = \mathbf{k} = 0$, and for the shape, with $\mathbf{p} \neq 0$.

D. Methodology for Form-Factor Shapes

In the past, a dipole parametrization has been used to fit experimental data and, also, lattice-QCD data:

$$F_A(q^2) = -\frac{g_A}{(1 - q^2/M_A^2)^2}. \quad (2.14)$$

Although a q^{-4} fall-off can be justified for asymptotically high q^2 , this form is **inconsistent with QCD in the region of interest**. It is also inadequate to describe electron-nucleon scattering data for $F_1(q^2)$ [25, 26]. The value at $q^2 = 0$ is well-known from neutron beta decay, $g_A = 1.2723(23)$ [27].

As neutrino scattering data have become more precise and the range of q^2 probed more diverse, different results for M_A have been reported. Among recent experiments, the NOMAD Collaboration [28] reports $M_A = 1.05 \pm 0.02 \pm 0.06$ GeV, while the MiniBooNE Collaboration [29] reports $M_A = 1.35 \pm 0.17$ GeV. These error bars do not reflect defects in the dipole parametrization.

Bhattacharya, Hill, and Paz [30] have proposed using a parametrization based on analyticity and unitarity. In the complex $t = q^2$ plane, $F_A(t)$ has a cut on the real axis for $t > t_{\text{cut}} \equiv 9M_\pi^2$ and is analytic elsewhere. One can map the q^2 plane onto the unit disk via.

$$z(t, t_{\text{cut}}, t_0) = \frac{\sqrt{t_{\text{cut}} - t} - \sqrt{t_{\text{cut}} - t_0}}{\sqrt{t_{\text{cut}} - t} + \sqrt{t_{\text{cut}} - t_0}}, \quad (2.15)$$

where t_0 can be chosen for convenience. This change of variables maps the cut to the unit circle; the small region for beta decay, $m_e^2 \leq t \leq (M_n - M_p)^2$, is mapped to a short interval of real z ; the scattering region $t < 0$ is mapped to another interval, which extends to $z \rightarrow 1$ as $t \rightarrow -\infty$. See Fig. 2 for an illustration. The endpoints of these intervals depend on t_0 .

Analyticity implies that the form factor can be expanded as a power series in z ,

$$F_A(q^2) = \sum_{k=0}^{\infty} a_k z(q^2, t_{\text{cut}}, t_0)^k, \quad (2.16)$$

and unitarity places a bound on the coefficients a_k , such that the expansion converges for $|z| < 1$. If an experiment or a lattice-QCD calculation accesses the range $-Q_{\text{max}}^2 \leq q^2 \leq 0$, then choosing.

$$t_0 = t_{\text{cut}} \left(1 - \sqrt{1 + Q_{\text{max}}^2/t_{\text{cut}}} \right) \quad (2.17)$$

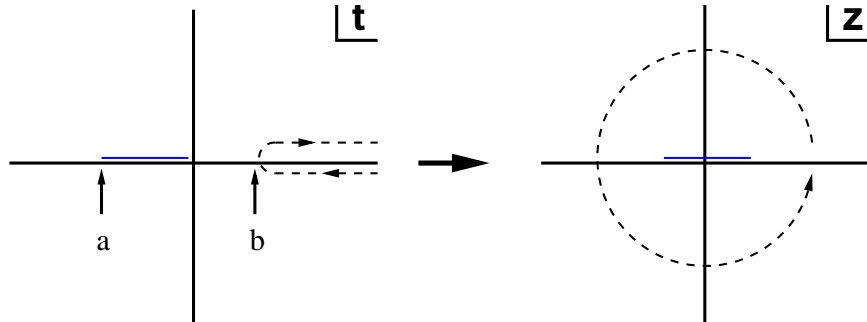


FIG. 2. The mapping of Eq. (2.15), which maps the whole complex t plane onto the unit disk in the complex z plane. The interval of real z for neutrino scattering is shown in blue. The point labeled “a” in the t plane corresponds to $-Q_{\text{max}}^2$; “b” to t_{cut} .

minimizes $|z|$, namely,

$$|z| \leq \frac{(1 + Q_{\max}^2/t_{\text{cut}})^{1/4} - 1}{(1 + Q_{\max}^2/t_{\text{cut}})^{1/4} + 1}. \quad (2.18)$$

For example, typical experiments reach $Q_{\max}^2 \approx 1.0 \text{ GeV}^2$, for which case $|z| \leq 0.24$, so quadratic and higher terms are naturally very small. Recently, this formalism has been applied to old bubble-chamber data for neutrino-deuteron scattering [31].

Following a successful procedure used by the Fermilab Lattice and MILC Collaborations in B physics [32–34], we will fit the lattice data to the z expansion. We plan to use the rest frame for the neutron, $\mathbf{k} = 0$, placed at the source in the discussion of Sec. II A. In this frame, the scattered proton should reach momenta up to $|\mathbf{p}|_{\max} = \sqrt{Q_{\max}^2} = 0.7 \text{ GeV}$. The box sizes of the HISQ ensembles lead to the quantum of momentum $2\pi/L = 0.21\text{--}0.25 \text{ GeV}$. Therefore, it seems sufficient to use $\mathbf{p} = 0$, $2\pi(1, 0, 0)/L$, and $2\pi(1, 1, 0)/L$. We will study whether we retain a signal at $2\pi(1, 1, 1)/L$. The output of the fit will be the first two or three coefficients a_k in Eq. (2.16), together with their errors and correlation matrix.

E. Blind Analysis of g_A

Our calculation of the normalization, g_A , is being done with a blinding factor. In our B - and D -physics calculations, we introduced blinding via a small but significant multiplicative offset in the perturbative matching factor. Here that simple scheme is not available. Instead, the three-point code multiplies all nucleon three-point data with an offset before writing out the file. The offset is known to no one, and only a few collaborators have the key needed to reveal it.

F. Related Calculations by Other Groups

Several collaborations around the world are pursuing calculations of nucleon form factors, including g_A . As mentioned above, most other efforts have box-size $L < 3 \text{ fm}$ for most, if not all, of the ensembles. In 2015, the European Twisted Mass collaboration published a result for g_A (and other zero-momentum matrix elements) at physical quark mass, albeit with $n_f = 2$ and only one lattice spacing [11]; the physical mass ensemble has $M_\pi L = 3$. The Mainz group [35] is extending its work on vector form factors to the axial current, using the CLS ensembles with $n_f = 2$ and (so far) $a \approx 0.05 \text{ fm}$, $M_\pi \approx 332 \text{ MeV}$, $M_\pi L = 4.0$. Within USQCD, there are efforts on clover ensembles [6] and on domain-wall ensembles [9]. The PNDME Collaboration is pursuing calculations of nucleon matrix elements on the HISQ ensembles, including g_A and form factors. They simulate valence quarks with the clover action, however. They have published results based on the nine HISQ ensembles with $a \approx 0.06, 0.09$, and 0.12 fm [36]. (At $a \approx 0.12 \text{ fm}$, PNDME used the middle volume.) Similarly, the CalLat Collaboration uses domain-wall fermions on the HISQ ensembles to obtain a precise value of g_A . [37]. Given the importance of these topics to both high-energy and nuclear physics, it is important, we believe, to have cross-checks and to make full use of the investments made in the HISQ ensembles.

III. CODE

We use the MILC code base [38], which is well known within USQCD. We extended the MILC code base to two- and three-point functions with the operators discussed in Sec. II A and continue

TABLE II. Timings to generate the HISQ zero-momentum two-point correlators on the physical-mass ensembles. These inversions account for the “1” in Eq. (2.10), i.e., 8 single-color inversions per configuration. We define kGPU = 1000 K40-GPU-hours and MJpsi = 10^6 Jpsi-core-hours.

$\approx a$ (fm)	$N_s^3 \times N_t$	N_{meas}	N_{left}	Inversions	2-pt tie-ups MJpsi	Status	When/Where
0.15	$32^3 \times 48$	3000		0.51 MJpsi	0.02	Done	AY 2016–17
0.12	$48^3 \times 64$	1000		5.25 MJpsi	0.03	Stopped	AY 2016–17
0.15	$32^3 \times 48$	1000		0.17 MJpsi	0.00	Stopped	AY 2016–17
0.12	$48^3 \times 64$	3000		3.15 MJpsi	0.09	Stopped	AY 2017–18
0.09	$64^3 \times 96$	4000		112.00 kGPU	1.64	Stopped	AY 2017–18
0.15	$32^3 \times 48$	3500	0	0.59 MJpsi	0.02	Done	AY 2016–18
0.12	$48^3 \times 64$	1000	0	1.05 MJpsi	0.03	Done	AY 2017–18
0.09	$64^3 \times 96$	1047	617	17.28 kGPU	0.43	Proposed	AY 2017–19
Total				17.28 kGPU	0.48	Proposed	AY 2018–19

TABLE III. Timings to generate the HISQ zero-momentum three-point correlators on the physical-mass ensembles. Here $N_{\text{mom}} = 1$, $N_{\text{cur}} = 2$, and $N_{\text{sep}} = 4$, leading to 192 single-color inversions. Timing estimates assume that the $a = 0.09$ fm propagators have previously been saved to tape.

$\approx a$ (fm)	$N_s^3 \times N_t$	N_{meas}	N_{left}	Inversions	2-pt tie-ups MJpsi	Status	When/Where
0.15	$32^3 \times 48$	3500	0	4.74 MJpsi	0.71	Done	AY 2017–18
0.12	$48^3 \times 64$	1000	980	62.72 kGPU	0.46	Running	AY 2017–19
0.09	$64^3 \times 96$	1047	1047	234.53 kGPU	13.23	Proposed	AY 2018–19
Total				297.25 kGPU	13.69	Proposed	AY 2018–19

to look for way to optimize. One of us belongs to the USQCD team working on staggered inverters, such as those reported in Ref. [39].

MILC inverters run on all relevant hardware, including GPU. The tie-ups are no different with the sequential propagators than with the approach of last year’s proposal. We are developing improvements to the MILC code that should speed up this part of the computation.

IV. RESOURCES

A. Timings and Resources Requested

Tables II–V summarize the time needed for separate components of the computation: two- and three-point correlators at zero and nonzero momentum. Table VI gathers the total for the four components. These estimates are more cost effective than before, thanks to USQCD software development and understanding the signal-to-noise problem of the old methodology. In particular, the QUDA library provides implementations of several solvers such as the flexible GMResDR and incremental eigCG solvers. The latter is designed for systems with many right-hand sides and includes a setup stage for the computation low-lying eigenvectors of the fermion matrix. While the eigenvalue deflation can reasonably accelerate the convergence rate, the number of eigenvectors

TABLE IV. Timings to generate $N_{\text{mom}} = 3$ HISQ nonzero momentum two-point correlators on the physical-mass ensembles. Timing estimates assume that the $a = 0.09$ fm propagators have previously been saved to tape.

$\approx a$ (fm)	$N_s^3 \times N_t$	N_{meas}	Inversions Tbyte	2-pt tie-ups MJ _{psi}	Status	When/Where
0.15	$32^3 \times 48$	3500		0.06	Proposed	AY 2018–19
0.12	$48^3 \times 64$	1000		0.10	Proposed	AY 2018–19
0.09	$64^3 \times 96$	1047	164.2	1.30	Proposed	AY 2018–19
Total			168.0	1.46	Proposed	AY 2018–19

TABLE V. Timings to generate the HISQ nonzero momentum three-point correlators on the physical-mass ensembles. For this table, we take $N_{\text{mom}} = 3$, $N_{\text{cur}} = 1$, and $N_{\text{sep}} = 4$, leading to — single-color inversions. Here we define kGPU = 1000 K40-GPU-hours and MJ_{psi} = one million J_{psi}-core-hours. Timing estimates assume that the $a = 0.09$ fm propagators have previously been saved to tape.

$\approx a$ (fm)	$N_s^3 \times N_t$	N_{meas}	Inversions kGPU	3-pt tie-ups MJ _{psi}	Status	When/Where
0.15	$32^3 \times 48$	3500	70.14	1.86	Proposed	AY 2018–18
0.12	$48^3 \times 64$	1000	96.00	1.01	Proposed	AY 2018–19
0.09	$64^3 \times 96$	1047	351.79	34.59	Proposed	AY 2018–19
Total			517.93	37.46	Proposed	AY 2018–19

TABLE VI. Summary and total allocations needed to complete the physics programs. Here we define kGPU = 1000 K40-GPU-hours and MJ_{psi} = one million J_{psi}-core-hours. Timing estimates assume that the $a = 0.09$ fm propagators have previously been saved to tape.

Component	Breakdown	Inversions kGPU	2 or 3-pt tie-ups MJ _{psi}	Tape storage (Tbyte)
2-pt ($p = 0$)	Table II	17.28	0.48	—
3-pt ($p = 0$)	Table III	297.25	13.69	—
2-pt ($p \neq 0$)	Table IV	0.00	1.46	164.2
3-pt ($p \neq 0$)	Table V	517.93	37.46	—
Total		832.46	53.09	0.99 MJ_{psi}
		\longrightarrow	240.56	\longleftarrow

required for the effective deflation scales with the problem size. One possible remedy to deal with large-volume systems with many right-hand sides is to exploit block-Krylov methods. Recently, Clark *et al.* extended the QUDA library with the block-optimized CG solver [39]. Contrary to the incremental eigCG solver, the block-CG method does not have a setup stage that has to be amortized. The use of blocks naturally generates more parallelism that makes block-Krylov methods very suitable algorithms for current and future HPC systems.

In total, we request 832 k K40-GPU-hours and 53 M J_{psi}-core-hours at BNL or Fermilab; we also request 50 Tbyte disk space and 168 Tbyte tape storage. We are still not completely satisfied with the time needed for the three-point tie-ups, which seem to be communications-bound, because

it scales poorly with the number of nodes in a job. If we can solve this problem, 53 M Jpsi-core-hours could be reduced. If we continue running at BNL and the tape storage has to be at Fermilab, some scratch space at Fermilab for staging is also needed. Using USQCD conversion factors, the total request is 241 M Jpsi-core-hours leading to a request of 241 M Jpsi-core-hours, at BNL or Fermilab.

With the tape back-up, we and other USQCD groups can use these data for other calculations. We ask that interested groups contact us to see whether the topics are of mutual interest.

B. Human Resources

This project constitutes the heart of Yin Lin’s Ph. D. research at the University of Chicago. Ciaran Hughes, a new postdoc at Fermilab is also part of the team. Alexei Strelchenko of the Fermilab Scientific Computing Division is our link to algorithm development.

V. RESULTS FROM 2015–2018

During allocation year (AY) 2015–2016, we explored how these calculations will work in practice, optimized the algorithms and codes, and obtained some preliminary results. The latter were presented at Lattice 2016 [40]. In AY 2016–2017, we have been studying the optimal number of noisy sinks, the range of source-sink separations, and increased the statistics from 1000 to 4000 configurations at $a \approx 0.15$ fm, leading to a (blinded) value of the axial charge: $\beta g_A = 1.45 \pm 0.22$ [41]. The error here is statistical and from one ensemble only, preventing a thorough study of systematics. At the end of AY 2016–2017 we decided to understand the reason for the poor statistics, leading to the new methodology discussed above.

The new strategy yields three-point correlators with small statistical uncertainties. Figure 3 shows a (blinded) zero-momentum correlator for four source-current separations, both in raw form and scaled by the fit to the two-point functions. Here we have 3400 measurements on the $a \approx 0.15$ fm ensemble, yielding uncertainties of order 10%.

As discussed above, we now have two-point data at three lattice spacings. A first look at the nucleon mass—with fits that are by no means optimized—is shown in Fig. 4.

VI. OUTLOOK

Eventually, we want to analyze all available physical-mass HISQ ensembles with $a \geq 0.06$ fm. Subsequently, we will examine other HISQ ensembles to carry out a finite-volume study at $a \approx 0.12$ fm and to connect our g_A with previous results at unphysical quark mass. In the longer term, other processes could be injected into Fig. 1, for example, $\nu n \rightarrow \ell^- \Delta^+$, nonresonant πp , and two-nucleon matrix elements of the form $\langle NN | A^\mu | NN \rangle$.

-
- [1] S. Ritz *et al.*, “Report of the Particle Physics Project Prioritization Panel,” (2014).
 - [2] “GENIE Neutrino Monte Carlo Generator,” <http://www.genie-mc.org/>.
 - [3] A. Bazavov *et al.* (MILC), *Phys. Rev. D* **87**, 054505 (2013), [arXiv:1212.4768 \[hep-lat\]](https://arxiv.org/abs/1212.4768).
 - [4] A. Bazavov *et al.*, (2017), [arXiv:1712.09262 \[hep-lat\]](https://arxiv.org/abs/1712.09262).

- [5] S. Capitani *et al.*, *Phys. Rev.* **D86**, 074502 (2012), arXiv:1205.0180 [hep-lat].
- [6] J. R. Green *et al.*, *Phys. Lett.* **B734**, 290 (2014), arXiv:1209.1687 [hep-lat].
- [7] B. J. Owen *et al.*, *Phys. Lett.* **B723**, 217 (2013), arXiv:1212.4668 [hep-lat].
- [8] R. Horsley *et al.*, *Phys. Lett.* **B732**, 41 (2014), arXiv:1302.2233 [hep-lat].
- [9] S. Ohta (RBC, UKQCD), PoS **LATTICE2014**, 149 (2015), arXiv:1410.8353 [hep-lat].
- [10] P. M. Junnarkar *et al.*, PoS **LATTICE2014**, 150 (2015), arXiv:1411.5828 [hep-lat].
- [11] A. Abdel-Rehim *et al.*, *Phys. Rev.* **D92**, 114513 (2015), (E) *Phys. Rev.* **D93**, 039904 (2016), arXiv:1507.04936 [hep-lat].
- [12] T. Yamazaki (PACS), PoS **LATTICE2015**, 081 (2016), arXiv:1511.09179 [hep-lat].
- [13] M. F. L. Golterman and J. Smit, *Nucl. Phys.* **B255**, 328 (1985).
- [14] J. A. Bailey, *Phys. Rev.* **D75**, 114505 (2007), arXiv:hep-lat/0611023 [hep-lat].
- [15] C. W. Bernard *et al.*, *Phys. Rev.* **D48**, 4419 (1993), arXiv:hep-lat/9305023 [hep-lat].

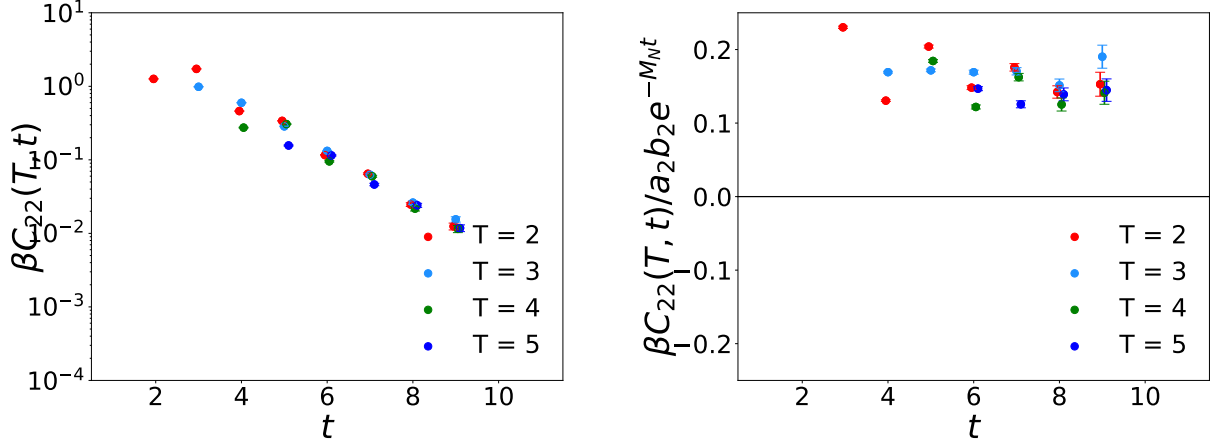


FIG. 3. Three-point correlation function $\beta C_{ij}^3(t, \tau)$ in the $(16, \frac{3}{2})$ irrep, where β is the blinding factor with four source-current separations, $\tau = 2$ (red), 3 (light blue), 4 (green), 5 (navy blue). Left: the correlator itself; right: the correlator scaled by $a_2 b_2 e^{-M_N t}$, where $a_2 b_2$ is the product of overlap factors from the fit and M_N the N -like mass from the fit. The fit is to the full matrix of two-point correlators shown in Fig. 5, $i = j = 2$. The full matrix of three-point correlators is shown in Fig. 6.

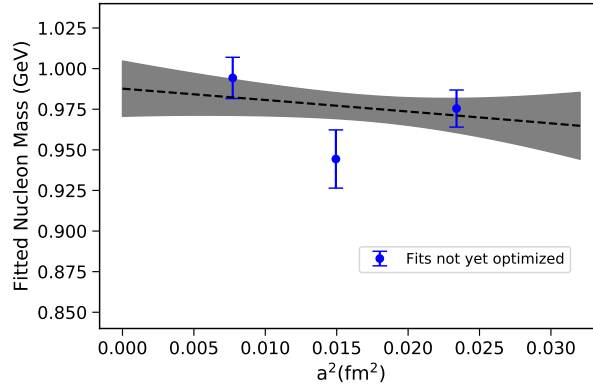


FIG. 4. Nucleon mass M_N vs. a^2 at three lattice spacings. The point at $a \approx 0.09$ fm has not reached full statistics, and all points are a work in progress vis a vis stability over time ranges chosen, etc.

- [16] C. W. Bernard *et al.*, *Phys. Rev.* **D64**, 054506 (2001), [arXiv:hep-lat/0104002 \[hep-lat\]](#).
- [17] H. Na, C. J. Monahan, C. T. H. Davies, R. Horgan, G. P. Lepage, and J. Shigemitsu (HPQCD), *Phys. Rev.* **D86**, 034506 (2012), [arXiv:1202.4914 \[hep-lat\]](#).
- [18] A. Bazavov *et al.* (Fermilab Lattice, MILC), *Phys. Rev.* **D87**, 073012 (2013), [arXiv:1212.4993 \[hep-lat\]](#).
- [19] C. McNeile and C. Michael (UKQCD), *Phys. Rev.* **D73**, 074506 (2006), [arXiv:hep-lat/0603007 \[hep-lat\]](#).
- [20] A. Bazavov *et al.* (Fermilab Lattice, MILC), “Standard model parameters and the search for physics beyond the standard model with HISQ,” (2018), proposal to USQCD.
- [21] A. Bazavov *et al.* (Fermilab Lattice, MILC), *Phys. Rev.* **D90**, 074509 (2014), [arXiv:1407.3772 \[hep-lat\]](#).
- [22] M. Lüscher, *JHEP* **1008**, 071 (2010), [arXiv:1006.4518 \[hep-lat\]](#).
- [23] S. Borsanyi *et al.* (Budapest-Marseille-Wuppertal), *JHEP* **1209**, 010 (2012), [arXiv:1203.4469 \[hep-lat\]](#).
- [24] A. Bazavov *et al.* (MILC), *Phys. Rev.* **D93**, 094510 (2016), [arXiv:1503.02769 \[hep-lat\]](#).
- [25] H. S. Budd, A. Bodek, and J. Arrington, (December, 2002), presented at the 2nd International Workshop on Neutrino-Nucleus Interactions in the Few GeV Region, [arXiv:hep-ex/0308005 \[hep-ex\]](#).
- [26] J. C. Bernauer *et al.* (A1), *Phys. Rev.* **C90**, 015206 (2014), [arXiv:1307.6227 \[nucl-ex\]](#).
- [27] C. Patrignani *et al.* (Particle Data Group), *Chin. Phys.* **C40**, 100001 (2016).
- [28] V. Lyubushkin *et al.* (NOMAD), *Eur. Phys. J.* **C63**, 355 (2009), [arXiv:0812.4543 \[hep-ex\]](#).
- [29] A. Aguilar-Arevalo *et al.* (MiniBooNE), *Phys. Rev.* **D81**, 092005 (2010), [arXiv:1002.2680 \[hep-ex\]](#).
- [30] B. Bhattacharya, R. J. Hill, and G. Paz, *Phys. Rev.* **D84**, 073006 (2011), [arXiv:1108.0423 \[hep-ph\]](#).
- [31] A. S. Meyer, M. Betancourt, R. Gran, and R. J. Hill, *Phys. Rev.* **D93**, 113015 (2016), [arXiv:1603.03048 \[hep-ph\]](#).
- [32] J. A. Bailey *et al.* (Fermilab Lattice, MILC), *Phys. Rev.* **D79**, 054507 (2009), [arXiv:0811.3640 \[hep-lat\]](#).
- [33] J. A. Bailey *et al.* (Fermilab Lattice, MILC), *Phys. Rev.* **D92**, 034506 (2015), [arXiv:1503.07237 \[hep-lat\]](#).
- [34] J. A. Bailey *et al.* (Fermilab Lattice, MILC), *Phys. Rev.* **D92**, 014024 (2015), [arXiv:1503.07839 \[hep-lat\]](#).
- [35] S. Capitani, M. Della Morte, D. Djukanovic, G. M. von Hippel, J. Hua, B. Jäger, P. M. Junnarkar, H. B. Meyer, T. D. Rae, and H. Wittig, (2017), [arXiv:1705.06186 \[hep-lat\]](#).
- [36] T. Bhattacharya, V. Cirigliano, S. Cohen, R. Gupta, H.-W. Lin, and B. Yoon (PNDME), *Phys. Rev.* **D94**, 054508 (2016), [arXiv:1606.07049 \[hep-lat\]](#).
- [37] E. Berkowitz *et al.*, (2017), and *Nature*, to appear, [arXiv:1704.01114 \[hep-lat\]](#).
- [38] MILC Collaboration, “MILC Code Version 7,” (2016).
- [39] M. A. Clark, A. Strelchenko, A. Vaquero, M. Wagner, and E. Weinberg, (2017), [arXiv:1710.09745 \[hep-lat\]](#).
- [40] A. S. Meyer, R. J. Hill, A. S. Kronfeld, R. Li, and J. N. Simone, *PoS LATTICE2016*, 179 (2017), [arXiv:1610.04593 \[hep-lat\]](#).
- [41] A. S. Meyer, *The nucleon axial form factor and staggered lattice QCD*, Ph.D. thesis, University of Chicago (2017).

APPENDIX: EXTRA FIGURES

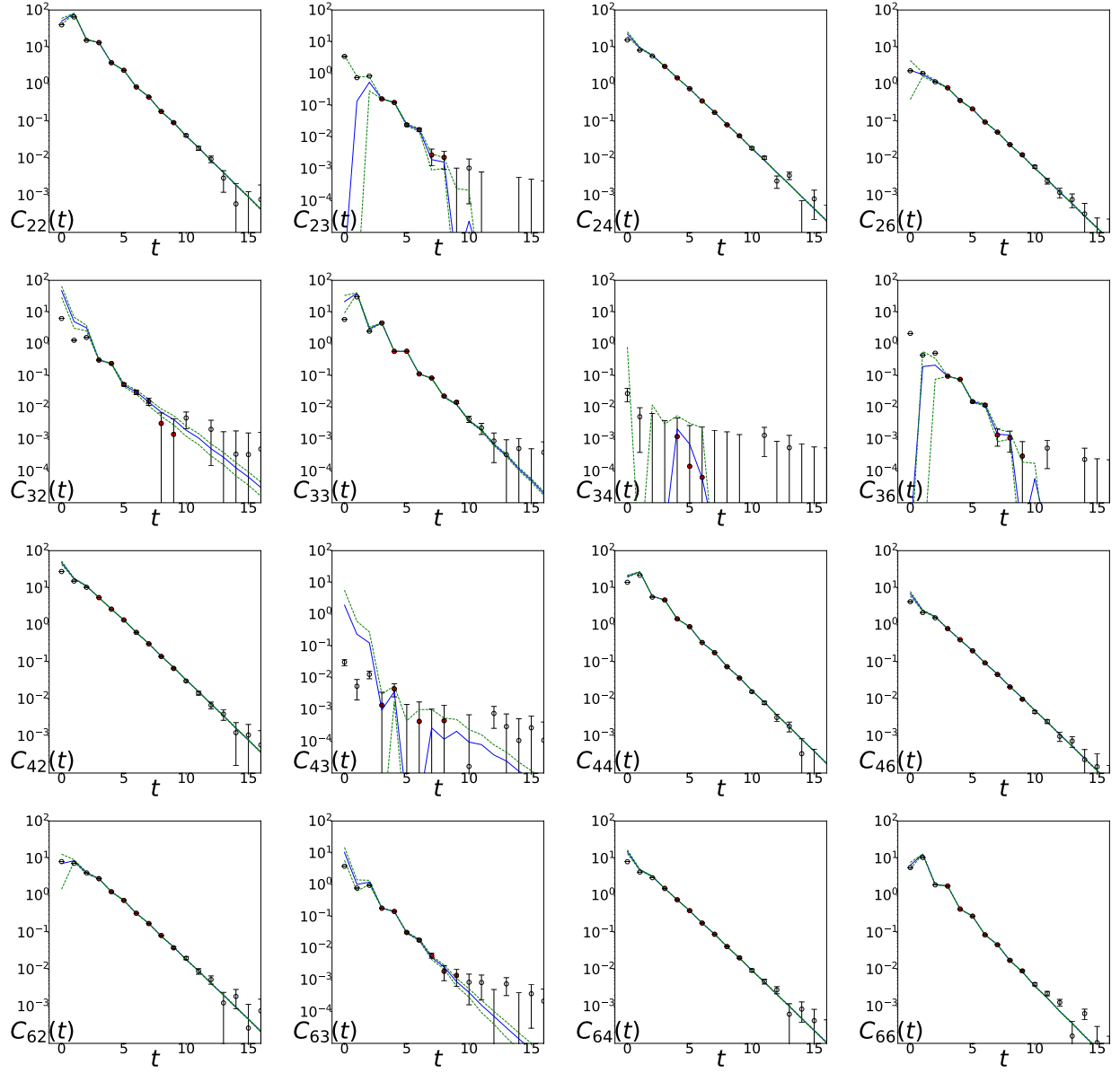


FIG. 5. Matrix of two-point correlation functions in the $(16, \frac{3}{2})$ irrep. Timeslices $4 \leq T \leq 9$ (filled in red) are included in the fit (red curve with green dashed error band).

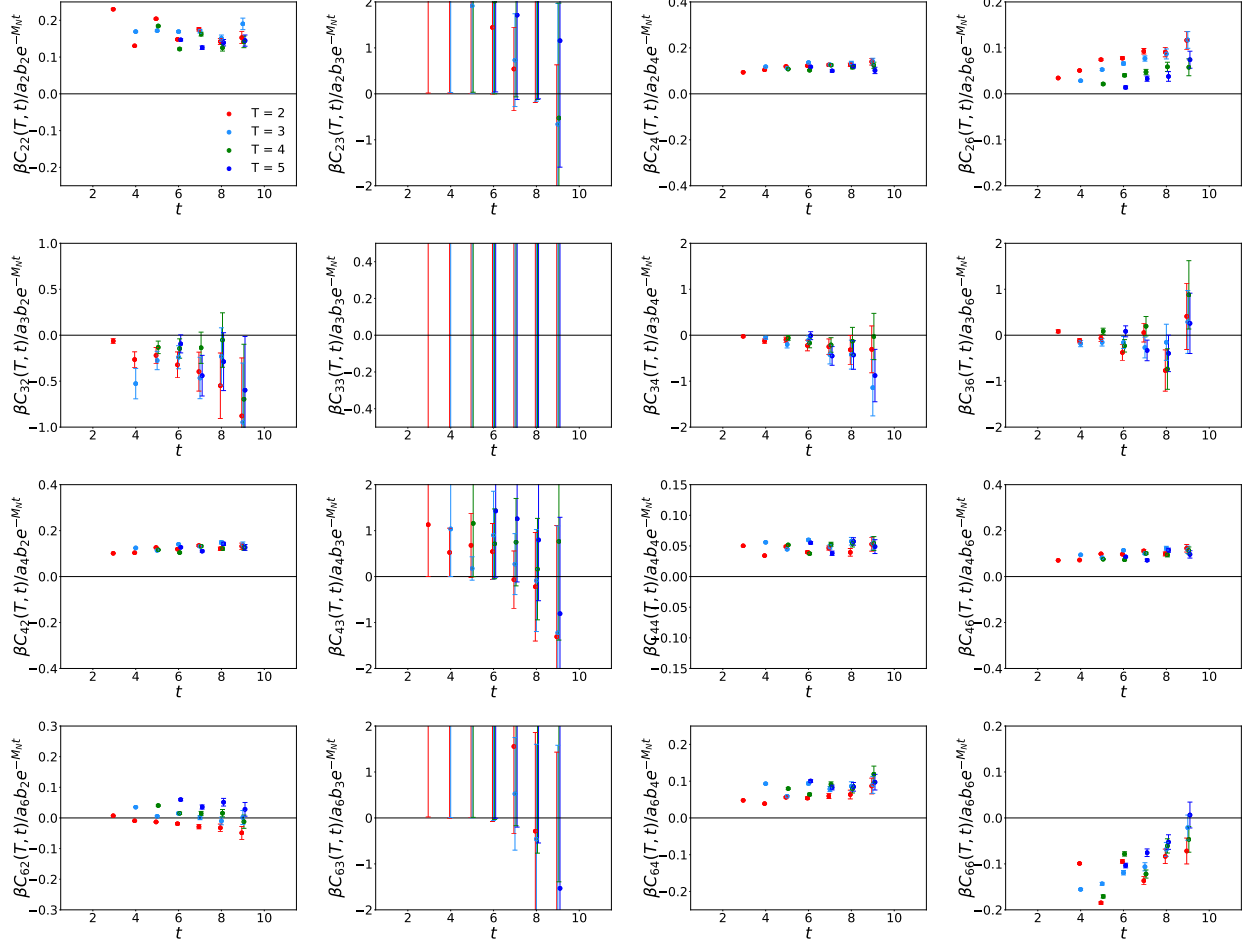


FIG. 6. Matrix of three-point correlation functions in the $(16, \frac{3}{2})$ irrep. Here the ratio $\beta C_{ij}^3(t, \tau)/e^{-M_N t}$ is plotted, where β is the blinding factor (unknown but stored in a lock box) and M_N is the N -like mass from fitting the two-point functions in Fig. 5. The four source-current separations are $\tau = 2$ (red), 3 (light blue), 4 (green), 5 (navy blue).